

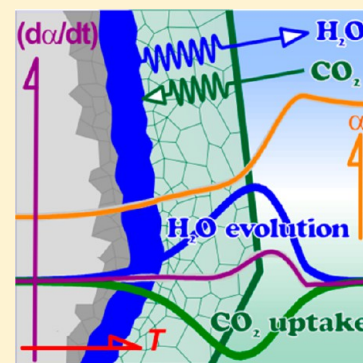
Phenomenological Kinetics of the Carbonation Reaction of Lithium Hydroxide Monohydrate: Role of Surface Product Layer and Possible Existence of a Liquid Phase

Yusuke Noda and Nobuyoshi Koga*

Chemistry Laboratory, Department of Science Education, Graduate School of Education, Hiroshima University, 1-1-1 Kagamiyama, Higashi-Hiroshima 739-8524, Japan

S Supporting Information

ABSTRACT: This article describes the physico-geometrical mechanism and overall kinetics for the carbonation of lithium hydroxide monohydrate (LHMH). The constituent reactions of thermal dehydration of LHMH and carbonation of as-produced anhydrous lithium hydroxide (LH) were investigated using thermogravimetry and morphological observations. On the basis of the kinetic information of the constituent reactions, the overall reaction of carbonation of LHMH under conditions of different CO₂ concentrations and heating rates was kinetically deconvoluted into separate processes of thermal dehydration and reaction of the as-produced LH with CO₂. The kinetic results were interpreted, with reference to the morphological characteristics of the partially reacted sample particles at different reaction stages, as the consecutive processes of the thermal dehydration of LHMH and the carbonation of as-produced LH starting at room temperature, which is geometrically controlled by shrinkage of the reaction interface, LHMH–LH–lithium carbonate (Li₂CO₃). The possible existence of a liquid phase at the reaction interface is deduced from the kinetic behavior and microscopic evidence. Variations in overall carbonation behavior as a function of heating rate and CO₂ concentration are explained by the changes in the gaseous diffusion behaviors for H₂O evolution and CO₂ uptake via the surface product layer of Li₂CO₃ and the evaporation rate of the liquid phase.

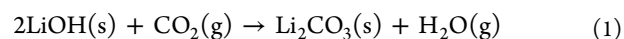


1. INTRODUCTION

Carbonation reactions of alkali and alkaline earth hydroxides and oxides have long been studied for the practical applications to decrease CO₂ concentration in a variety of reaction environments. In recent years in particular, the solid–gas carbonation reactions have been extensively studied as one of the potential methods to capture CO₂ from industrial combustion sources and air to mitigate the greenhouse effect.^{1–8} A few newly proposed CO₂ absorbents include alkaline silicates,^{9,10} aluminates,^{11,12} and zirconates.^{13–15} Kinetic studies of the solid–gas reactions for CO₂ capture and their reverse reactions for recycling the absorbents are fundamental for practical applications,^{10–12,14–20} in addition to thermodynamic considerations. Generally, the reaction kinetics of solid–gas reactions for CO₂ capture show complex behavior sensitively influenced by properties of the solid reactants and reaction conditions.^{21–26} Because of the heterogeneous nature of the reactions, the formation of a surface product layer of carbonates around the reacting particles at the beginning of a reaction is unavoidable.^{27,28} The nature of the surface product layer varies depending on the reaction conditions, and it changes as the reaction advances through growth of product crystals or sintering.²⁹ Because the surface product layer plays an important role in regulating the diffusion of gaseous species taking part in the reaction, the overall kinetics of the carbonation reaction is thus controlled by the physico-geometrical properties of the surface product layer and the

local self-generated reaction conditions. In this respect, reaction morphology and physico-geometrical kinetic behavior of a single reacting particle or grain are fundamental information for interpreting the overall kinetics in a reaction system of an assemblage of many reacting particles. This information may also be useful for simulating the reaction behaviors on a larger scale, for instance, at a pilot plant capturing CO₂.

The present study focuses on the carbonation reaction of a lithium hydroxide (LH)–CO₂–H₂O system. It is known that the solid–gas reaction between LH and CO₂ has been practically used to remove CO₂ in life support systems in spacecraft and submarines.³⁰



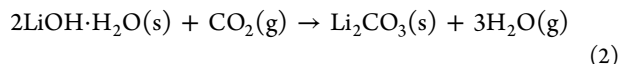
The irreversible and exothermic reaction to form lithium carbonate (Li₂CO₃) occurs at room temperature with a high absorption capacity because of the low molar mass of the absorbent, LH. As in the carbonation reaction of Ca(OH)₂ extensively studied,^{1,4,16,18,19,21,22,26,29} the physico-geometrical mechanism of the reaction seems to be so complex, as CO₂ must diffuse into the reacting particle and product water vapor must diffuse away from the reacting particle through the

Received: January 11, 2014

Revised: February 11, 2014

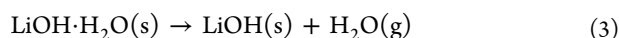
Published: February 20, 2014

generated surface product layer. In such a physico-geometrical reaction scheme, the properties of the surface product layer significantly affect the kinetic behavior of the reaction. In addition, the reaction is reported to be accelerated by atmospheric water vapor.^{31–33} Formation of lithium hydroxide monohydrate (LHMH) as an intermediate compound has been postulated to explain the effect of water vapor on the reaction.^{31–33} In a contrary finding, it was recently reported by Zho et al.³⁴ that the reaction rate of LH carbonation is more than 10 times higher than that for LHMH. In the case of using LHMH as the CO₂ absorbent, the amount of water vapor generated (eq 2) is three times larger than the amount generated by LH (eq 1).



It has also been reported that the reaction of LHMH with CO₂ is kinetically controlled by the thermal dehydration of LHMH and smoothly advances without a barrier product layer for the temperatures lower than 333 K.³⁴ For this reaction, the rate behavior might be influenced largely by diffusional removal of water vapor from the reacting particle and possible self-generated reaction conditions by the evolved water vapor. The possible existence of a liquid phase inside the reacting particles of LHMH during the reaction with CO₂ has also been suggested.³⁴

In this study, the kinetics of the reaction of LHMH with CO₂ under linearly increasing temperature were investigated to study the interrelationship between the properties of the surface product layer and the diffusion processes for CO₂ uptake and H₂O evolution and those changes depending on the reaction conditions. For collecting fundamental information related to the reaction of eq 2, the kinetic behavior of thermal dehydration of single crystalline particles of LHMH (eq 3) was revealed by thermoanalytical measurements and microscopic observations.



In addition, changes in the rate behavior of the reaction of the as-produced LH with CO₂ (eq 1) as a function of reaction temperature and CO₂ concentration were followed by mass change measurements and were interpreted with the aid of morphological observations of the reacting particles. Based on those findings, an interpretation of the changes in the reaction behavior of the LHMH carbonation under linearly increasing temperature depending on heating rate and CO₂ concentration by modeling the kinetics of CO₂ uptake and H₂O evolution was attempted.

2. EXPERIMENTAL SECTION

2.1. Characterization of Sample. Reagent grade lithium hydroxide monohydrate (LHMH, Sigma-Aldrich, Japan) was used without any further purification. The sample particles were sieved to different particle size fractions, 90–150, 150–300, 300–500, and 500–1000 μm, using sieves with different meshes and a shaking apparatus (MVS-1, As-One Co.). The powder X-ray diffraction (XRD) pattern of the sample was recorded using a diffractometer (RINT2200 V, Rigaku Co.) with Cu Kα radiation (40 kV, 20 mA). The morphologies of the sample particles were observed using a stereomicroscope (Olympus SZX7). The thermogravimetry–differential thermal analysis (TG–DTA) curves for a 5.0 mg sample, weighed in a platinum pan (6φ × 2.5 mm), were recorded at a heating rate β

of 5 K min^{−1} in flowing N₂ (80 cm³ min^{−1}) using a TG–DTA instruments (DTG-50M, Shimadzu Co.).

2.2. Thermal Dehydration of Lithium Hydroxide Monohydrate. Using a hanging-type TG instrument (TGA-50M, Shimadzu Co.), the mass loss curves for the thermal dehydration of LHMH were recorded in flowing N₂ (80 cm³ min^{−1}) by heating a 5.0 mg sample, weighed in a platinum pan (6φ × 2.5 mm), at different heating rates (1 ≤ β ≤ 10 K min^{−1}). The phase change of the sample, press-fitted on a platinum plate without grinding, during the thermal dehydration of LHMH in flowing N₂ (100 cm³ min^{−1}) was traced by high temperature XRD (HTXRD) using the above diffractometer, which was equipped with a programmable heating chamber (PTC-20A, Rigaku Co.). The XRD measurement was repeated every 25 K while heating the sample from room temperature to 473 K at a β of 10 K min^{−1}, keeping the sample temperature constant during the diffraction measurements for 15 min. Partially dehydrated samples were prepared by heating the sample particles in the above TG instrument to different temperatures at a constant β of 5 K min^{−1} under the same conditions as the mass loss measurements. A portion of the partially dehydrated sample particles was observed using scanning electron microscopy (SEM; JSM-6510, Jeol) after coating the sample with platinum by sputtering (20 mA, 60 s) using a deposition apparatus (JFC-1600, Jeol). The residual portion of partially dehydrated sample particles was fixed using a synthetic mounting agent (Matsunami Glass Ind. Co.). After the mounting agent solidified, thin sections of the partially dehydrated sample particles were prepared by polishing the inclusion body using abrasive papers (nos. 500–2000), and the thin sections were observed under polarized light using an optical microscope (Olympus, BH-2).³⁵

2.3. Reaction of Lithium Hydroxide with Carbon Dioxide. Changes in crystalline phase during the reaction of LH with CO₂ were traced by HTXRD using the following procedure. The LHMH sample, press-fitted to a platinum plate without grinding, was heated to 573 K at a β of 10 K min^{−1} in flowing N₂ (60 cm³ min^{−1}) and then was cooled to either 523 or 323 K at a rate of −10 K min^{−1}. After stabilizing the sample temperature for 5 min, CO₂ (40 cm³ min^{−1}) was added to the flowing gas. The diffraction measurement immediately started and was repeated every 13 min. The LHMH sample (500–1000 μm, 5.0 mg) was weighed in a platinum pan (6φ × 2.5 mm) and was heated to 573 K in flowing N₂ (60 cm³ min^{−1}) using the above TGA-50M to obtain LH. The as-produced LH was subsequently cooled in the instrument to different temperatures (573–303 K) at a rate of −5 K min^{−1}. After stabilizing the sample temperature for 5 min, CO₂ was introduced to the reaction chamber at a rate of 40 cm³ min^{−1}, in addition to the purge gas of N₂ (60 cm³ min^{−1}), to record the mass change due to the reaction of LH with CO₂. In another set of experiments, the same procedure was performed, but the CO₂ concentration in the mixed N₂–CO₂ gases introduced into the reaction chamber was varied from 10% to 50%. The LH samples reacted partially with CO₂ were obtained by interrupting the above mass change measurements at 323, 473, and 573 K at different reaction times. The morphologies of the partially reacted samples were observed by SEM after coated with Pt by sputtering.

2.4. Reaction of Lithium Hydroxide Monohydrate with Carbon Dioxide. The mass change traces for the reaction of LHMH with CO₂ were recorded by heating the LHMH sample (500–1000 μm, m₀ = 5.0 mg), weighed in a

platinum pan ($6\phi \times 2.5$ mm), in the above TGA-50M instrument at β of 5 K min^{-1} in flowing a $\text{N}_2\text{--CO}_2$ mixed gas with different CO_2 concentrations (ranging from 40% to 80%) at a rate of $100 \text{ cm}^3 \text{ min}^{-1}$. Similarly, the mass change traces at different heating rates ($1 \leq \beta \leq 10 \text{ K min}^{-1}$) were recorded in a flow of a $\text{N}_2\text{--CO}_2$ mixed gas (40% CO_2) at a rate of $100 \text{ cm}^3 \text{ min}^{-1}$. Morphologies of the partially reacted samples were studied by interrupting the mass change measurements and observing the samples by SEM after coating with sputtered platinum. The HTXRD measurements for the reaction of LHMH with CO_2 were performed in a flow of mixed $\text{N}_2\text{--CO}_2$ gas (40% CO_2) at a rate of $100 \text{ cm}^3 \text{ min}^{-1}$ by heating the sample to 523 K at a β of 10 K min^{-1} . The XRD measurements were started every 25 K under the conditions otherwise identical to those for the thermal dehydration of LHMH as described above.

3. RESULTS AND DISCUSSION

3.1. Characterization of Sample. The XRD pattern of the LHMH sample was in agreement with a simulated diffraction peaks based on the reported crystal structure of LHMH (monoclinic, S.G. = $\text{C}2/m$, $a = 7.4153$, $b = 8.3054$, $c = 3.1950$, and $\beta = 110.107^\circ$) and with JCPDS 25-0486.³⁶ The XRD pattern is illustrated in Figure S1 in the Supporting Information. The sample particles were single crystals and rhombohedra in shape (Figure S2).

Figure 1 shows TG–derivative TG (DTG)–DTA curves for the LHMH sample ($500\text{--}1000 \mu\text{m}$, $m_0 = 5.0 \text{ mg}$) recorded at β

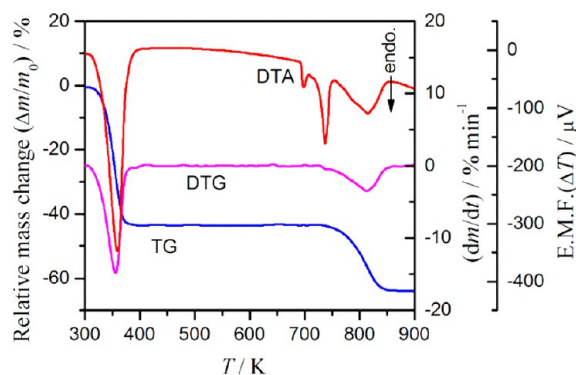
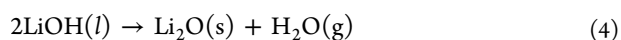


Figure 1. TG–DTG–DTA curves for the LHMH sample ($500\text{--}1000 \mu\text{m}$, $m_0 = 5.0 \text{ mg}$) recorded at $\beta = 10 \text{ K min}^{-1}$ in flowing N_2 ($80 \text{ cm}^3 \text{ min}^{-1}$).

$= 10 \text{ K min}^{-1}$ in flowing N_2 ($80 \text{ cm}^3 \text{ min}^{-1}$). On heating, the sample decomposes in two mass loss steps. The first mass loss step starts from room temperature and is complete at a temperature lower than the boiling point of water. The mass loss value is in agreement with the calculated value (-42.9%) according to eq 3.

Before the second mass loss step, two endothermic peaks are found at approximately 700 and 720 K in the DTA curve without any correlated mass change. These endothermic phenomena are interpreted as the structural phase transition and melting of LH, respectively.^{37,38} The subsequent mass loss step is ascribed to the thermal decomposition of molten LH according to the reaction:



The observed mass loss value for the second mass loss step is close to the calculated value (-21.5% with reference to LHMH).

3.2. Thermal Dehydration of Lithium Hydroxide Monohydrate. Through the thermal dehydration of crystalline water of LHMH according to eq 3, the crystalline structure of the sample change to the tetragonal phase of anhydrous LH (S.G. = $\text{P}4/nmm$, $a = 3.549$, and $c = 4.334$)³⁹ without indicating any intermediate crystalline phases (Figure S3). The mass loss traces for thermal dehydration of the sample recorded at a constant β shifted to higher temperature with increasing particle size (Figure S4). This is a typical trend of the contracting-geometry-type reaction, because the longer distances of the linear advancement of the reaction interface are required for the larger particles to completing the reaction.

Kinetics of the thermal dehydration process was analyzed by the mass loss traces at different β (Figure S5). Figure 2 illustrates the kinetic rate data for the thermal dehydration of LHMH and the step-by-step results in the kinetic analysis process. The kinetic rate data, converted from the mass loss traces by normalizing to fractional reaction, systematically shift to higher temperatures with increasing β (Figure 2a), irrespective of the particle size fraction in the LHMH sample. For analyzing the kinetic rate data, the following fundamental kinetic equation was assumed:^{40,41}

$$\frac{d\alpha}{dt} = A \exp\left(-\frac{E_a}{RT}\right) f(\alpha) \quad (5)$$

where α , A , E_a , and R are the fractional reaction, the Arrhenius preexponential factor, the apparent activation energy, and the gas constant, respectively. The kinetic model function $f(\alpha)$ incorporates the physico-geometrical characteristics of the reaction. Using the kinetic rate data for different β , apparent E_a values at different α were determined according to Friedman method⁴² by the plots of $\ln(d\alpha/dt)$ versus reciprocal temperature, T^{-1} (Figure 2b). The isoconversional plots indicate a linear relationship irrespective of α , and this was observed for all samples with different particle sizes. Slopes of the plots did not show any significant variation with α and among the samples with different particle sizes.

The apparent E_a values calculated from the slopes are shown in Figure 2c. During the initial stage of the reaction ($\alpha \leq 0.1$), E_a value is observed to decrease, especially for samples of smaller particle sizes. The contribution of surface reaction to the overall kinetics is a possible explanation for this variation in E_a . The established reaction ($0.1 \leq \alpha \leq 0.9$) is characterized by a constant E_a , independent of the particle size. The average E_a in the range $0.1 \leq \alpha \leq 0.9$ are listed in Table 1. The large fluctuation observed in the final stage of the reaction ($\alpha \geq 0.9$) was attributed as a result of the diffusional removal of the trapped water vapor or liquid water within the product solid, which is discussed later with the results of the morphological observations.

As far as the main reaction part ($0.1 \leq \alpha \leq 0.9$), the fundamental kinetic equation for the single step reaction, eq 5, can be applied because of the linear relationship of the isoconversional plot and constant E_a . Then, an experimental master plot can be formalized by introducing the Ozawa's generalized time, θ :^{41,43,44}

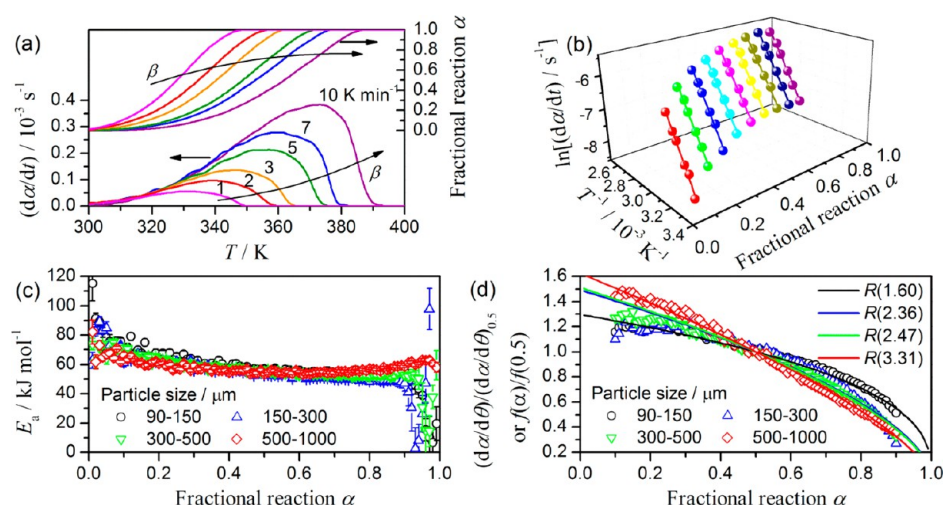


Figure 2. Kinetic rate data for the thermal dehydration of LHMH and step-by-step results in the kinetic analysis process. (a) Kinetic rate data at different β (500–1000 μm sample), (b) Friedman plots at different α from 0.1 to 0.9 in steps of 0.1 (500–1000 μm sample), (c) E_a values at different α , and (d) experimental master plots and fitting curves using $R(n)$ model.

Table 1. Kinetic Results for the Thermal Dehydration of LHMH Samples

particle size/ μm	$E_a/\text{kJ mol}^{-1}$	A/s^{-1}	n	R^{2a}
500–1000	56.8 ± 2.8	$(3.06 \pm 0.04) \times 10^5$	3.31 ± 0.06	0.9951
300–500	56.6 ± 4.7	$(4.35 \pm 0.05) \times 10^5$	2.47 ± 0.04	0.9903
150–300	54.7 ± 5.2	$(2.67 \pm 0.07) \times 10^5$	2.36 ± 0.09	0.9509
90–150	58.5 ± 5.8	$(1.62 \pm 0.01) \times 10^6$	1.60 ± 0.01	0.9871

^aDetermination coefficient of the nonlinear least-squares analysis for $f(\alpha)$ versus α plot.

$$\frac{d\alpha}{d\theta} = \frac{d\alpha}{dt} \exp\left(\frac{E_a}{RT}\right) = Af(\alpha) \quad \text{with}$$

$$\theta = \int_0^t \exp\left(-\frac{E_a}{RT}\right) dt \quad (6)$$

The normalized experimental master plots of $(d\alpha/d\theta)/(d\alpha/d\theta)_{0.5}$ versus α^{45} are shown in Figure 2d. Although shapes of the experimental master plots systematically change with changes in sample particle size, the kinetic model function for the phase-boundary-controlled reaction model, $R(n)$,⁴⁶ fits the experimental master plot irrespective of the particle size:

$$R(n): f(\alpha) = n(1 - \alpha)^{1-1/n} \quad (7)$$

where the kinetic exponent, n , describes the dimension of reaction interface shrinkage. The kinetic parameters for thermal dehydration of the LHMH samples, determined through a nonlinear least-squares fit according to the $R(n)$ model,⁴⁷ are also summarized in Table 1. The variation in the shape of the experimental master plots is correlated to changes in n , which gradually rises to 3 with increasing particle size. The variation in n can be interpreted as follows: because the same sample mass was used for each set of particle sizes, the sample particles with smaller sizes formed a denser sample layer in the sample cell. Under such condition, gross diffusion of evolved water vapor via the sample layer is difficult, resulting in a possible gradient of water vapor pressure in the assemblage of sample particles and a distribution of the fractional reaction among the particles.^{48–51} In this scenario, a single particle based kinetic model, as described by eqs 5–7, cannot be directly applied to the kinetic rate data because of the possible distribution of α among the sample particles.⁵² For the sample particles with the

largest size (500–1000 μm), n close to 3 indicates the applicability of the ideal single particle-based kinetic model.

Prior to the microscopic observations of the product LH morphology, it was confirmed by the mass change measurement for the thermal dehydration process and the cooling process of the product LH in flowing air that the reaction of LH with CO_2 in air at room temperature during the time required for preparation of microscopic observations could be neglected (Figure S6). Figure 3 shows typical microscopic views of the partially dehydrated sample particles. The surface product layer shows a stacking structure of plate-like crystals (Figure 3a). Each plate is an aggregate of densely arranged and sintered submicrometer-sized crystals of LH (Figure 3b). Thus, diffusion of water vapor produced at the internal reaction sites is possibly blocked by the surface product layer. In each plate of the surface product layer, several holes with several micrometers in diameter are observed (Figure 3c). These holes can be interpreted as the diffusion channels for product water vapor. The single crystalline reactant solid covered with the surface product layer is clearly observable on the thin section of the partially dehydrated sample particles (Figure 3d). All surfaces are already covered by the surface product layer before the reaction reaches $\alpha \approx 0.1$. This is evidence for a contracting geometry-type reaction, which was expected from the shifting of the mass-loss trace with particle size.

From the above observations, it is postulated that the thermal dehydration of LHMH particles is a physico-geometrically controlled process, which initiates on the surface by nucleation and growth of the solid product and subsequently proceeds by advancement of the reaction interface produced between the reactant crystal and the surface product layer toward the center of the reactant crystal. Based on the kinetic obedience to the phase-boundary-controlled reaction model, the linear advance-

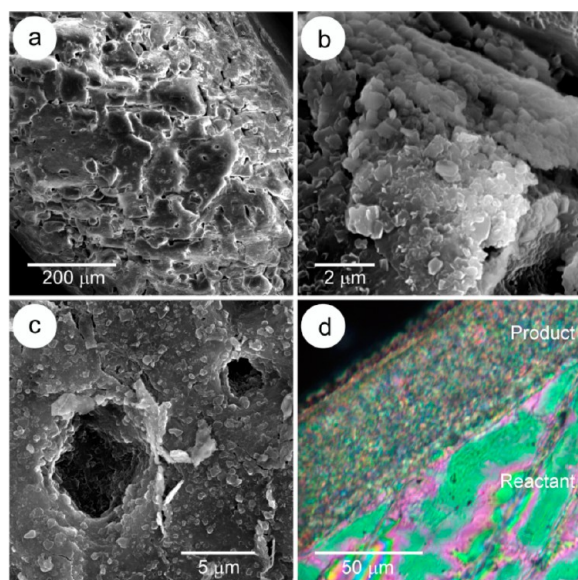


Figure 3. Typical microscopic views of partially dehydrated LHMH particles (500–1000 μm) after heating to different temperatures at $\beta = 5 \text{ K min}^{-1}$ in flowing N_2 (80 $\text{cm}^3 \text{ min}^{-1}$). (a–c) SEM images of the surfaces (353 K, $\alpha = 0.63$) and (d) a polarizing microscopic view of a thin section (323 K, $\alpha = 0.07$).

ment rate of the reaction interface is controlled by a chemical reaction with $E_a \approx 55\text{--}60 \text{ kJ mol}^{-1}$. Geometry of the interface shrinkage can be deduced as approximately three-dimensional from the microscopic observations and $n \approx 3$ in the phase-boundary-controlled reaction model determined for the LHMH samples with the largest particle size. Although there is a diffusion path for the product water vapor through the holes in the surface product layer, the process may become difficult as the reaction advances because the necessary diffusion path increases as the reaction proceeds. In the final stage of the reaction, the diffusion path may be labyrinthine, and the water vapor could be trapped in the product layer. This may be the possible explanation for the large fluctuation of the apparent E_a in the final stage of the reaction. This assumption is supported by the observation of a separated mass loss step in the final stage at higher temperatures (Figure S7).

From the above observations for the thermal dehydration of LHMH, it was confirmed that the kinetic behavior of a single LHMH particle can be deduced from the mass change measurements for the sample with particles sized 500–1000 μm under the experimental conditions employed in this study. We thus decided to perform mass change measurements for the carbonation reactions of LHMH and LH, as described in the following sections, using the same amount of sample mass, 5.0 mg, and particle size, 500–1000 μm .

3.3. Reaction of Lithium Hydroxide with Carbon Dioxide. The solid products obtained by reacting LH with CO_2 at different constant temperatures (303–573 K) was identified as Li_2CO_3 (monoclinic, S.G. = $C2/c$, $a = 8.39$, $b = 5.00$, $c = 6.21$, and $\beta = 114.5^\circ$)⁵³ (Figure S8). At a constant temperature, the reaction initiated with a sudden mass gain irrespective of the CO_2 concentration used (which varied from 10% to 50%), but the mass change of the subsequent process was largely dependent on the CO_2 concentration (Figure S9). The time-resolved XRD during the reaction at 323 and 523 K indicates the transformation of LH to Li_2CO_3 without producing any intermediate crystalline phases (Figure S10).

Figure 4 shows the mass change traces for the reaction with a CO_2 concentration of 40% at different temperatures. The total

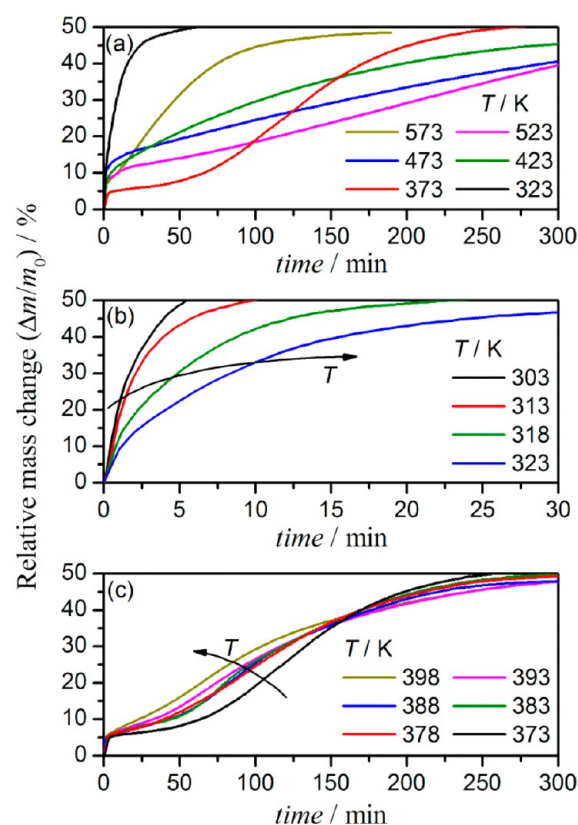


Figure 4. Isothermal mass change traces for the reaction of LH with CO_2 at different temperatures in flowing $\text{N}_2\text{--CO}_2$ mixed gas (40% CO_2). (a) 323–573, (b) 303–323, and (c) 373–398 K.

mass gain by the reaction, $50.7 \pm 2.1\%$, was more than 90% of the value calculated according to eq 1: 54.3%. A complex temperature dependence of the mass change rate, which is not Arrhenius-type behavior, is observed (Figure 4a). An important observation is the very large reaction rate at temperatures lower than 323 K. In this temperature range, the mass change rate increases with decreasing temperature (Figure 4b). In a temperature range between 373 and 398 K, the mass change rate increases with temperature in the first half of the reaction (Figure 4c). The inversion phenomenon of the temperature dependence of the mass change rate again appears for the reaction in the temperature range 423–523 K. The complex temperature-dependent change in the overall reaction rate could not be simply explained by thermodynamic or kinetic considerations.

Figure 5 shows SEM images of partially reacted samples under different conditions. The final products produced at 323 K (Figure 5a) and 573 K (Figure 5b) show different surface textures. Formation of a surface product layer that covers the product particles is a characteristic of the final product at 573 K. At 573 K, the reaction initiates with a rapid mass gain that suddenly changes to a slower mass gain process at approximately $\alpha = 0.15$ (Figure 4a). For the reaction at a temperature higher than 373 K, all of the final products indicated similar surface product layers, and the reaction processes were characterized by a sudden change in the rate behavior at α between 0.09 and 0.22. In contrast, a smooth

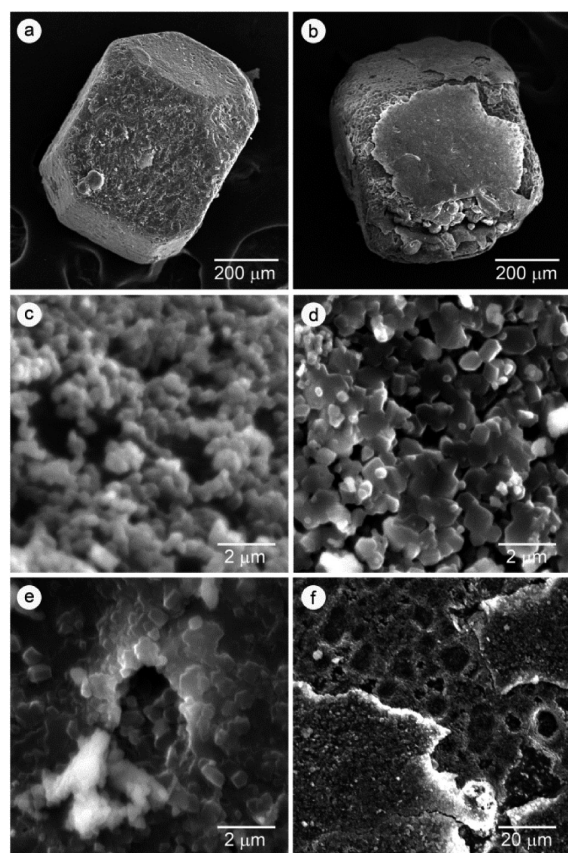


Figure 5. Typical SEM images of surface textures of the solid product obtained by the reaction of LH with CO_2 (40%). (a) Final product (Li_2CO_3) produced by the isothermal heating at 323 K, (b) final product (Li_2CO_3) produced by isothermal heating at 573 K, (c) enlarged surface texture of panel a, (d) surface texture of the sample partially reacted by isothermal heating at 473 K ($\alpha = 0.24$; just after the initial mass-gain process), (e) final product (Li_2CO_3) produced by isothermal heating at 473 K, and (f) enlarged surface texture of panel b.

mass gain during the reaction is observed for 323 K (Figure 4a,b). Aggregates of submicrometer-sized product particles on the surface of the final product at 323 K are confirmed (Figure 5c). At the same time, micrometer-sized holes that are possible diffusion channels for water vapor removal and CO_2 intake are also observed. The differences between the surface product layers formed at 573 and 323 K may be responsible for the differences in rate behavior.

To track the changes in the surface product layer during carbonation, the surface textures of the sample particles at different stages in the reaction at 473 K were compared. Figure 5d,e are the reacting samples just after the initial rapid mass gain and the final product, respectively. In the former, the crystals in the surface product layer are the size of a micrometer and have sintered. The final surface product layer shows further sintering. A number of holes are visible in the well-sintered surface product layer, which perhaps are diffusion channels during the latter half of the reaction. For a portion of the final product produced at 573 K, the surface product layers were cleaved, and the internal surfaces were exposed (Figure 5f). The internal surfaces have many crater-like concavities. It is suspected that higher water vapor pressures are generated inside the particles during the reaction. Liquid water formation and evaporation through holes in the surface product layer is a

possible mechanism for the development of the crater-like concavities.

Formation of the outer shell of surface product layer at the beginning of the reaction during the initial mass gain process controls the subsequent reaction of LH with CO_2 . At temperatures lower than 323 K, the surface product layer is composed of poorly defined crystalline particles of Li_2CO_3 and that have possible diffusion channels for water vapor removal and CO_2 intake during the subsequent reaction. The outer shell formation at a temperature higher than 373 K, significantly impedes the subsequent reaction, resulting in the sudden arrest of the rapid mass gain process at the beginning of the reaction. Outer shells of surface product layers with a similar “orange peel” appearance have been reported for the thermal decomposition and dehydration of inorganic solids.^{54–56} After the formation of the “orange peel”, the internal reaction advances under self-generated reaction conditions, which are controlled by the formation rate of the gaseous product and diffusional removal through “orange peel”. In this reaction, CO_2 diffusion toward the internal reaction sites is an additional factor controlling the self-generated reaction conditions.

Because formation of this type of outer shell is not observed for temperatures lower than 323 K, the inverse temperature effect on the overall reaction rate observed in this temperature region (Figure 4b) should be explained by another factor. As one of the possible causes of the inverse temperature effect, liquid phase formation inside each reacting particle, which results directly from the reaction between LH and CO_2 or through the condensation of the evolved water vapor, can be proposed as has been already suggested by Zho et al.³⁴ The effect of atmospheric water vapor on the acceleration of the reaction rate has been reported in many previous studies for this reaction in an LH sample bed.^{31–33} The acceleration effect has been explained by the possible formation of LHMH as an intermediate compound and the higher reactivity of LHMH with CO_2 . However, in this study, no intermediate crystalline phase could be detected during the reaction (Figure S10), irrespective of the reaction temperature. In addition, the possible formation of intermediate LHMH does not account for the inverse temperature effect on the reaction rate. If a liquid phase, presumably an aqueous LH solution, exists at the reaction interface, CO_2 is easily absorbed in the solution, and the as-formed carbonic acid dissociates to carbonate ion. Formation of Li_2CO_3 thus proceeds as mediated by the liquid phase. Accordingly, this process shows kinetic advantages for CO_2 uptake and the formation of Li_2CO_3 . With decreasing reaction temperature, condensation of evolved water vapor is promoted, and the evaporation of water vapor from the as-produced solution becomes suppressed, generating a larger amount of liquid phase inside each particle. In this model, a higher reaction rate is expected at lower temperatures because of the larger amount of interfacial liquid phase. The reaction mechanism involving the existence of liquid-like layer of water in the reacting solids has also been proposed for the carbonation reaction of $\text{Ca}(\text{OH})_2$.^{4,18,21}

3.4. Reaction of Lithium Hydroxide Monohydrate with Carbon Dioxide. Figure 6 shows TG–DTG curves for the reaction of LHMH with CO_2 in flowing mixed N_2 – CO_2 gas ($100 \text{ cm}^3 \text{ min}^{-1}$) with varying CO_2 concentrations under a linearly increasing temperature, $\beta = 5 \text{ K min}^{-1}$. Despite the large variation in the mass-change behaviors depending on the CO_2 concentration, the final mass-change value is nearly identical among the measurements. The average mass change

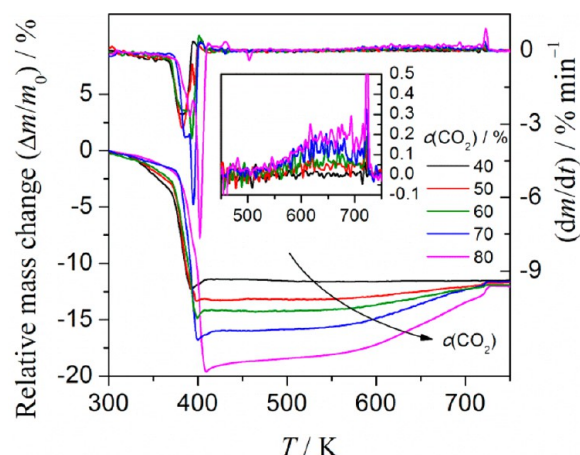


Figure 6. TG–DTG curves ($\beta = 5$ K min^{−1}) for the reaction of LHMH (500–1000 μm, $m_0 = 5.0$ mg) with CO₂ in flowing mixed N₂–CO₂ gas (100 cm³ min^{−1}) with different CO₂ concentrations.

value, $-11.6 \pm 0.4\%$, agrees with the calculated value, -12.0% , according to the reaction described by eq 2. Irrespective of the CO₂ concentration, the mass loss initiates at room temperature. It should be noted that the mass loss rate is higher for the reaction under lower CO₂ concentration for temperatures lower than 373 K, i.e., the boiling point of water. At higher temperatures, the reaction shows a rapid mass loss process irrespective of CO₂ concentration. The drastic change in the reaction behavior at the boiling point of water is another indication of the possible existence of liquid water in the reacting particles at temperatures lower than the boiling point. The mass loss value at this stage systematically increases with increasing CO₂ concentration; thus, the minimum sample mass during the reaction is observed for the reaction using the highest CO₂ concentration. The minimum value of sample mass during the reaction is larger than the calculated value for the thermal dehydration of LHMH (eq 3). This indicates that the reaction of LH and CO₂ has already occurred at temperatures lower than the boiling point of water. On further heating, the sample gains mass because of the reaction of LH with CO₂. The mass gain curve shifts to higher temperatures with increasing CO₂ concentration. At approximately 720 K, which is the melting point of LH, the sample mass reaches that of the final product, Li₂CO₃.

Figure 7 shows changes in the XRD pattern of the LHMH sample during stepwise isothermal heating in flowing mixed N₂–CO₂ gas (40%–CO₂). At 323 K, XRD peaks of LHMH are already significantly attenuated (Figure 7a), and XRD peaks attributed to LH and Li₂CO₃ appear (Figure 7b). Thus, thermal dehydration of LHMH and the reaction of the as-produced LH with CO₂ simultaneously occur right from the beginning of the overall reaction. At 373 K, almost all the XRD peaks attributed to LHMH and LH have disappeared, and the major XRD peaks are because of Li₂CO₃. In the light of the mass change behavior observed above, the overall reaction is not completed at this temperature. It is assumed that the XRD pattern at 373 K is due to the formation of a surface Li₂CO₃ layer with a significant thickness. There are no distinguishable changes in the XRD pattern for higher temperatures; therefore, it can be assumed that any reactions at temperatures higher than 373 K are internal. This observation implies that the overall reaction is influenced by the impedance effect of the surface product layer

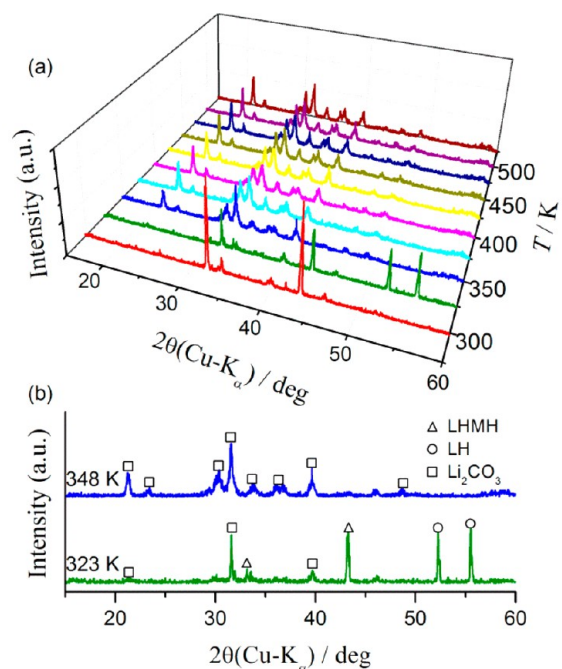


Figure 7. Changes in the XRD patterns of LHMH (500–1000 μm) during stepwise heating in flowing mixed N₂–CO₂ gas (40%–CO₂, 100 cm³ min^{−1}). (a) From room temperature to 523 K and (b) at 323 and 348 K.

on the diffusional removal of the product water vapor and CO₂ intake for the internal reaction.

Figure 8 shows SEM images of the surface textures of LHMH partially dehydrated and reacted with CO₂ in flowing mixed N₂–CO₂ gas (40 or 80%–CO₂, 100 cm³ min^{−1}) under a linearly increasing temperature, $\beta = 5$ K min^{−1}. Successive changes in the surface texture of the sample after thermal dehydration and reaction with CO₂ (80%) are illustrated in Figure 8a–e. At the beginning of the reaction at 333 K, the particle surfaces are covered with product crystals (Figure 8a). From the above observations of the XRD patterns, the surface product could be Li₂CO₃. At 413 K, where the mass change behavior turns from mass loss to mass gain (Figure 8b,c), a core–shell structure is formed on the sample particle, which is coated with a compact Li₂CO₃ layer (Figure 8c). The surface layer obviously blocks the diffusional removal of the product water vapor from inside, as in the case of “orange peel” in the thermal decomposition of solids.^{54–56} In this reaction, the layer also obstructs the diffusion of CO₂ from the outside for the internal reaction. The swelling up and bursting of the surface product layer observed in Figure 8b could be due to rapid escape of the internal water vapor. This interpretation is supported by the rapid mass loss process observed around the boiling point of water in the mass change measurements. On the inside of the outer shell, well-grown whiskers and plate-like crystals of Li₂CO₃ are observed (Figure 8d). Such crystal growth of Li₂CO₃ seems to be promoted by the presence of liquid phase inside the particle at the temperature lower than the boiling point of water. Thus, the rapid mass loss process could have been triggered by the boiling of water. The surface texture of the final product (773 K, Figure 8e) is comparable with that reacted partially (Figure 8c). This is another indication that the mass gain process at higher temperatures is due to an internal reaction. In the surface product layer of the final product under lower CO₂ concentration (40%, Figure 8f),

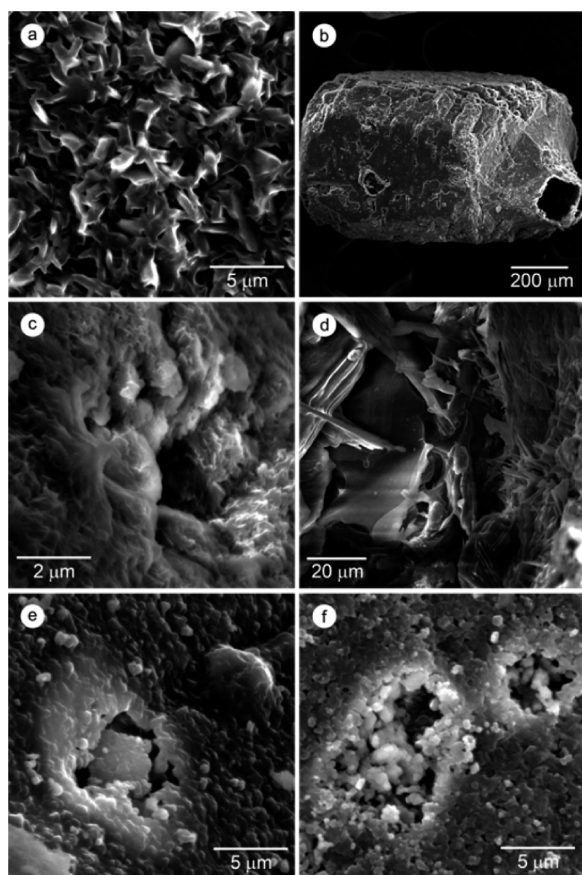


Figure 8. Typical SEM images of the surface textures of the LHMH sample (500–1000 μm) partially dehydrated and reacted with CO_2 by heating the sample at $\beta = 5 \text{ K min}^{-1}$ in flowing mixed $\text{N}_2\text{--CO}_2$ gas (40 or 80% CO_2 , $100 \text{ cm}^3 \text{ min}^{-1}$). (a) At the very beginning of the reaction heated to 333 K in 80% CO_2 , (b–d) heated to 413 K in 80% CO_2 , (e) final product (Li_2CO_3) obtained by heating to 773 K in 80% CO_2 , and (f) final product (Li_2CO_3) obtained by heating to 773 K in 40% CO_2 .

a large number of pores can be found. These pores are possible diffusion channels for product water vapor and reactant CO_2 . The variation in the mass change behavior under different CO_2 concentrations is interpreted by the changes in the compactness in the structure of the surface product layer with a smoother reaction process under lower CO_2 concentrations.

Figure 9 shows TG–DTG curves for the reaction of LHMH and CO_2 in flowing mixed $\text{N}_2\text{--CO}_2$ gas (40% CO_2 , $100 \text{ cm}^3 \text{ min}^{-1}$) at different β . The shape of the TG curve systematically changes depending on β . With increasing β , the first-half mass loss shifts to higher temperatures. The rapid mass loss around the boiling point of the possible liquid phase is characteristic of the reaction at higher β . The mass gain process at the final stage of the reaction is only observed for those reactions with a rapid mass loss process around the boiling point of water.

In order to simulate the mass change behavior at different β , we deconvoluted the overall mass change process into two different reaction processes: the thermal dehydration of LHMH, process $i = 1$, and the reaction of LH with CO_2 , $i = 2$. When those reaction processes are assumed to be independent, the kinetic equation can be expressed as the weighted summation of those reaction processes.^{57–61}

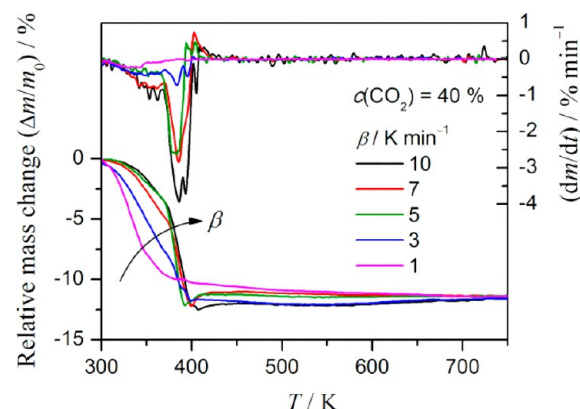


Figure 9. TG–DTG curves for the reaction of LHMH (500–1000 μm , $m_0 = 5.0 \text{ mg}$) with CO_2 in flowing mixed $\text{N}_2\text{--CO}_2$ gas (40% CO_2 , $100 \text{ cm}^3 \text{ min}^{-1}$) at different β .

$$\frac{d\alpha}{dt} = \sum_{i=1}^N c_i A_i \exp\left(-\frac{E_{a,i}}{RT}\right) f_i(\alpha_i) \quad \text{with} \quad \sum_{i=1}^N c_i = 1$$

$$\text{and} \quad \sum_{i=1}^N c_i \alpha_i = \alpha \quad (8)$$

where N is the number of processes; in this case $N = 2$. The parameters c_i , A_i , $E_{a,i}$, and α_i are the contribution ratio to the overall reaction rate, the apparent value of the Arrhenius preexponential factor, the apparent activation energy, and the fractional reaction, respectively, for each process i . For the kinetic model function $f_i(\alpha_i)$ for the process i , the empirical kinetic model function of Sesták–Berggren model, $\text{SB}(m, n, p)$,⁶² was employed for both processes in order to accommodate any possible deviations from the conventional physico-geometrical kinetic models.^{62–66}

$$\text{SB}(m, n, p): \quad f(\alpha) = \alpha^m (1 - \alpha)^n [-\ln(1 - \alpha)]^p \quad (9)$$

where m , n , and p are the kinetic exponents. For the mathematical optimization of all the parameters in eqs 8 and 9, default values of the parameters were determined using the following: (1) The c_i values were calculated based on the stoichiometry of the constituent reactions according to eqs 1–3: $c_1 = 3.59$ and $c_2 = -2.59$; (2) for the thermal dehydration of LHMH ($i = 1$), all the kinetic parameters were set by the formal kinetic analysis of the experimental data, as explained earlier (Table 1); (3) For the reaction of LH with CO_2 ($i = 2$), the kinetic exponents in the SB model were set to $\text{SB}(0, 1, 0)$ corresponding to a first-order reaction; (4) the value of $E_{a,2}$ was systematically set to a reasonable value ranging from 50 to 160 kJ mol^{-1} , and the value of $A_{i,2}$ was determined for each value of $E_{a,2}$ by graphically comparing $(d\alpha/dt)$ versus time for the experimental mass change traces and fitting according to eqs 8 and 9. Then, an optimization was run to minimize F , the squared sum of the difference between the experimental data for $(d\alpha/dt)_{\text{exp}}$ versus time and $(d\alpha/dt)_{\text{cal}}$ versus time calculated from eqs 8 and 9.

$$F = \sum_{j=1}^M \left[\left(\frac{d\alpha}{dt} \right)_{\text{exp},j} - \left(\frac{d\alpha}{dt} \right)_{\text{cal},j} \right]^2 \quad (10)$$

where M is the number of data points.

Figure 10 graphically illustrates the results of the kinetic simulation. The curve fitting results were mostly independent

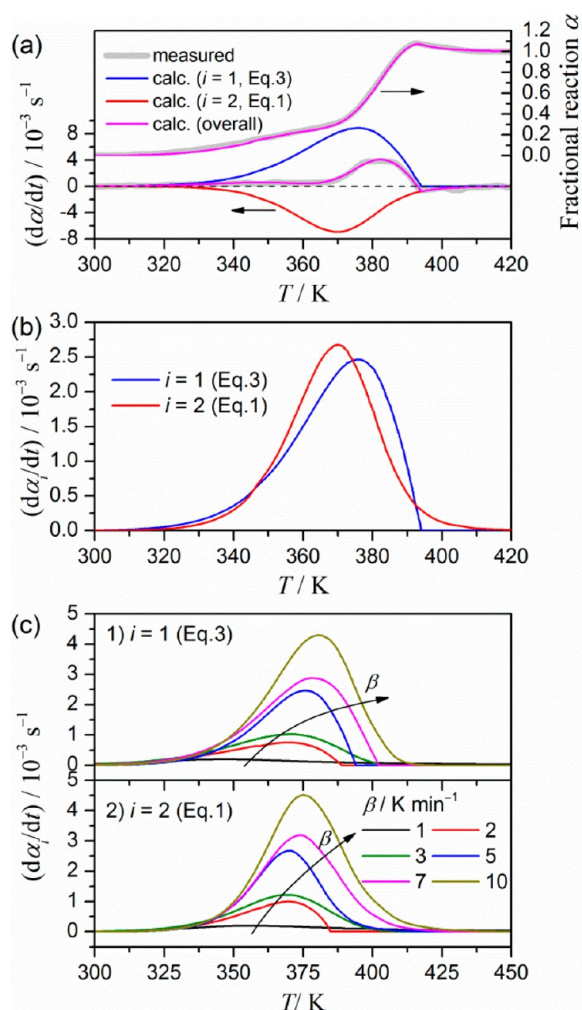


Figure 10. Results of the kinetic deconvolution for the reaction of LHMH (500–1000 μm) with CO_2 in flowing N_2 – CO_2 mixed gas (40%– CO_2) at different β divided into two different processes: 1) thermal decomposition of LHMH ($i = 1$) and 2) the reaction of LH with CO_2 ($i = 2$, default $E_{a,2} = 60 \text{ kJ mol}^{-1}$). (a) Typical result for the reaction at $\beta = 5 \text{ K min}^{-1}$, (b) comparison between the kinetic rate data ($\beta = 5 \text{ K min}^{-1}$) deconvoluted into the thermal dehydration of LHMH and the reaction of LH with CO_2 , and (c) change in the deconvoluted kinetic rate data with β .

of the assumed $E_{a,2}$ as the default value for process $i = 2$ (Figure 10a). In addition, changes in the optimized parameters as a function of β were not significant. Table S1 lists the optimized kinetic parameters for all the cases as a function of the value chosen for the default $E_{a,2}$. The optimized Arrhenius parameters for process $i = 1$ are not largely influenced by the default $E_{a,2}$, whereas those for $i = 2$ indicate significant correlation with the optimized $E_{a,2}$ as shown in Figure S11. It should be noted that it is very difficult to ascribe physical significance to optimized parameters that indicate mutual correlations, i.e., a kinetic compensation effect.^{67–70} In this study, the optimized parameters are treated as mathematical parameters for fitting the experimental kinetic rate curves because the curve fitting results were not largely influenced in spite of the mutually correlated changes in the parameters. The results obtained by the optimization using the default $E_{a,2} = 60 \text{ kJ mol}^{-1}$, which is comparable with the fixed value for the default $E_{a,1}$, were selected to deconvolute the processes (Figure 10a) because the

reaction of the as-produced LH with CO_2 ($i = 2$) occurs in the same temperature region as the thermal dehydration of LHMH ($i = 1$).

For the simulated kinetic curves for the processes $i = 1$ and 2, slight changes in the reaction temperature can be observed accompanying different shapes of the kinetic curves (Figure 10b). Thermal dehydration of LHMH ($i = 1$) is the preceding event at the initial part, as is expected from the sequential order of the reaction processes. However, the reaction of LH and CO_2 ($i = 2$) initiates as soon as the thermal dehydration of LHMH starts and LH is produced on the surface of the reactant particles. The appearance of the XRD peaks of Li_2CO_3 at the beginning of the reaction, as observed in Figure 7, supports that supposition. The reactions proceed as consecutive processes, but the reaction of LH with CO_2 has a higher acceleration rate and gets ahead of the thermal dehydration of LHMH; therefore, the observed phenomena cannot be explained by an assumption of consecutive reactions of the thermal dehydration of LHMH and the reaction of the as-produced LH with CO_2 . The existence of a liquid phase in the reactant particles during the reaction, as supported by SEM observations of the reacting particles (Figure 8) and the rate behavior of the reaction between LH and CO_2 , is one of the possible causes of the inversion phenomenon. The possibility of the existence of a liquid phase at the reaction interface for the reaction of LHMH with CO_2 is higher than that for the reaction of LH with CO_2 , because of the evolution of water vapor due to the thermal dehydration of LHMH and the reaction of the as-produced LH with CO_2 . The reaction of the as-produced LH with CO_2 peaks at a temperature lower than that for the thermal dehydration of LHMH at a temperature near the boiling point of the solution (Figure 10b). The rapid evaporation of water decelerates the reaction of LH and CO_2 . During the rapid mass loss process, the counter diffusion of CO_2 through the surface product layer also becomes difficult. After the thermal dehydration of LHMH is complete, residual LH reacts with CO_2 to complete the overall reaction. With increasing β , the residual amount of LH in the reacting particle at the instance of completion of the thermal dehydration of LHMH increases, and the mass gain curve for the reaction of LH with CO_2 shifts to higher temperatures. The different trends in temperature shift with increasing β for the thermal dehydration of LHMH and the reaction of the as-produced LH with CO_2 result in a systematic change in the mass change behavior of the overall reaction (Figure 10c).

When assuming the existence of a liquid phase during the reaction, the exact origin of the evolved water vapor cannot be discerned. To simulate the process, we further divided the reaction of LH with CO_2 into two processes: (1) CO_2 uptake and (2) H_2O evolution. Then, the kinetic simulation was refined by assuming three mass change steps for the thermal dehydration of LHMH ($i = 1$), CO_2 uptake by the reaction of LH with CO_2 ($i = 2a$), and the evolution of H_2O by the same reaction ($i = 2b$). For the kinetic simulation procedure as described above, the contributions of the respective reaction steps, c_i , were determined by the reaction stoichiometry. The results of the previous kinetic simulation, listed in Table S1, were used for the other kinetic parameters. The kinetic parameters for the three different reaction steps after optimization are summarized in Table S2. We observed no significant differences between the kinetic parameters derived here and those determined previously. Therefore, to sum up the H_2O evolution, the overall reaction was simulated with

dividing into (1) H₂O evolution (a sum of $i = 1$ and $i = 2b$) and (2) CO₂ uptake ($i = 2a$), as shown in Figure S12. The rate behavior of the overall process is satisfactorily simulated by the H₂O evolution and CO₂ uptake processes (Figure S12a). The estimated difference between the peak temperatures for the H₂O evolution and CO₂ uptake processes is smaller than that estimated from the kinetic simulation by assuming the two chemical reaction processes of eqs 3 and 1 (Figure S12b), but the peak for the CO₂ uptake still appears before that of H₂O evolution process. The dependence of the overall reaction behavior on β is also explained by the different rate behaviors of the H₂O evolution and CO₂ uptake processes and their variation with respect to β (Figure S12c).

To account for the variation of reaction behavior depending on CO₂ concentration shown in Figure 6, a similar kinetic approach via kinetic deconvolution was used. For reactions under higher CO₂ concentrations, the reaction of LH with CO₂ had two distinguishable temperature regions. Therefore, for the kinetic simulation, we assumed three reaction steps: (1) the thermal dehydration of LHMH ($i = 1$), (2) the reaction of LH with CO₂ ($i = 2$) taking place in the lower temperature region accompanying the thermal dehydration of LHMH, and (3) the latter stage of the reaction of LH with CO₂ that occurs at the higher temperatures ($i = 3$). The parameter values for the kinetic deconvolution were set as described in the previous simulations. The details of the results for the kinetic simulation for the three reaction steps are described in Figure S13 and Tables S3 in the Supporting Information. In summary, the curve fitting results were not largely influenced by the arbitrarily selected values for $E_{a,2}$ and $E_{a,3}$. However, the optimized parameters depended on CO₂ concentration, especially the kinetic exponents in SB(m,n,p).

The result of the kinetic simulation was further refined by dividing the reaction of LH with CO₂ into CO₂ uptake and H₂O evolution processes, i.e., by dividing $i = 2$ into $i = 2a$ and $2b$ and $i = 3$ into $i = 3a$ and $3b$, where a and b denote CO₂ uptake and H₂O evolution, respectively. In addition, the reaction process describing the overall CO₂ uptake and H₂O evolution was simulated. Figure 11 shows typical results for the kinetic simulation for CO₂ uptake (the sum of $i = 2a$ and $3a$) and H₂O evolution processes (the sum of $i = 1, 2b$, and $3b$), which were obtained by setting default E_a for the reaction of LH with CO₂ to 60 kJ mol⁻¹. The simulated curve satisfactorily fit the experimental curve irrespective of the CO₂ concentration, as shown in Figure 11a for the reaction under 60%-CO₂. The optimized parameters for the reaction under different CO₂ concentrations are listed in Table S4. For temperatures below 450 K, where the thermal dehydration of LHMH and the reaction of as-produced LH and CO₂ concurrently occur, the CO₂ uptake initiates slightly in delaying from the H₂O evolution and peaks at a lower temperature than the H₂O evolution (Figure 11b). The behavior is practically identical to that for 40%-CO₂ at different β (Figures 10 and S12). For temperatures higher than 500 K, the CO₂ uptake is simulated as the preceding process to the H₂O evolution (Figure 11b insert), which describes the sequence in the reaction of LH with CO₂. With increasing CO₂ concentration, trends of decelerations of both the H₂O evolution and CO₂ uptake are observed for the lower temperature process (Figure 11c). Furthermore, the reaction temperature shifts to higher temperatures for CO₂ concentrations greater than 70%. The temperature difference between the peaks for the H₂O evolution and CO₂ uptake increases with increasing CO₂

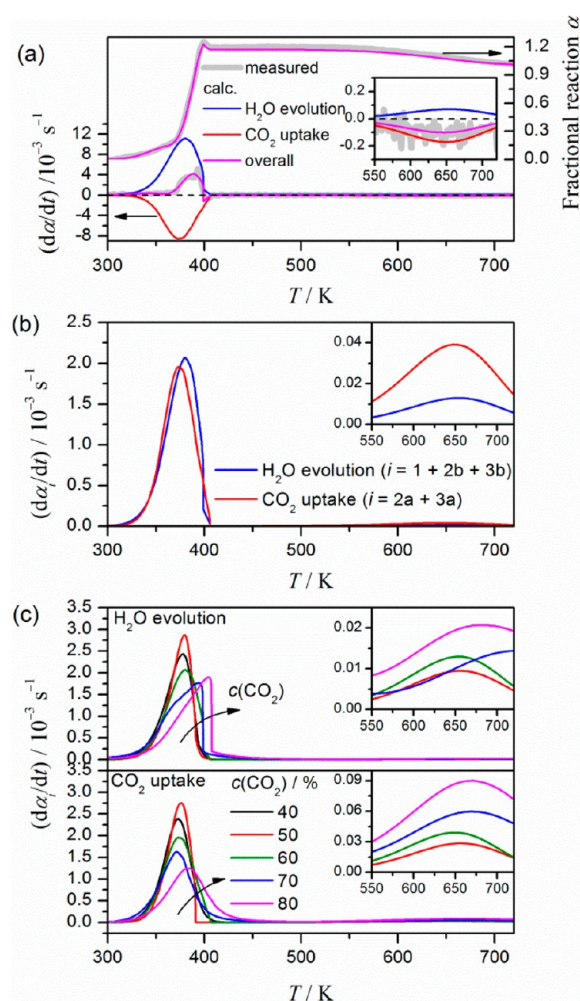


Figure 11. Results of the kinetic simulation of the CO₂ uptake and H₂O evolution processes during the reaction of LHMH (500–1000 μm) with CO₂ at $\beta = 5 \text{ K min}^{-1}$ in flowing mixed N₂–CO₂ gas with varying CO₂ concentration. (a) Typical result for the reaction under 60%-CO₂, (b) comparison between the simulated kinetic rate curves for H₂O evolution and CO₂ uptake under 60%-CO₂, and (c) changes in the simulated kinetic rate curves for H₂O evolution and CO₂ uptake with changes in CO₂ concentration.

concentration. This indicates a systematic decrease in the contribution of the reaction of LH with CO₂ to the simultaneous processes of the thermal dehydration of LHMH and the reaction of LH with CO₂ with increasing CO₂ concentration, resulting in an increase in the residual LH available to react with CO₂ at higher temperatures (Figure 11c insert). The variation in the overall reaction behavior with CO₂ concentration can be explained by a change in the property of the surface product layer of Li₂CO₃. The dense surface product layer produced under higher CO₂ concentrations impedes the CO₂ diffusion from the atmosphere to the internal reaction interface, resulting in an increase of the residual LH that reacts with CO₂ at the higher temperatures.

4. CONCLUSIONS

Thermal dehydration of LHMH crystalline particle is well described by a three-dimensional phase-boundary-controlled reaction with $E_a = 55\text{--}60 \text{ kJ mol}^{-1}$. The reaction of as-produced LH (from thermal dehydration of LHMH) with CO₂ has very complex rate behavior, which changes depending on

reaction temperature and CO₂ concentration. The rate behavior cannot simply be explained by kinetics or thermodynamics but is understood by considering the changes in the properties of the surface product layer of Li₂CO₃ as a function of reaction temperature and CO₂ concentration. Changes in the blocking of gaseous diffusion for CO₂ intake and H₂O evolution by the surface product layer result in a variation of the self-generated local reaction conditions. At a temperature lower than 323 K, the rate of carbonation of LH increases with decreasing temperature. Existence of a liquid phase at the reaction interface that moves to the center of the sample particle is a possible explanation for the inverse effect of temperature on the reaction rate.

The carbonation of LHMH crystalline particles proceeds by the thermal dehydration of LHMH and the accompanying carbonation of as-produced LH. Under linearly increasing temperature, these two reactions are successive processes that initiates at room temperature. According to the kinetic behavior for thermal dehydration of LHMH, the successive process initially progresses by the movement of the reaction interface, LHMH–LH, toward the center of the particle. By the subsequent process of the carbonation of as-produced LH, the surface product layer of Li₂CO₃ is immediately generated. Property of the surface product layer associated with the gaseous diffusions depends on CO₂ concentration in the reaction atmosphere. Blocking of diffusional removal of water vapor, produced by the thermal dehydration of LHMH and the reaction of LH with CO₂, by the surface product layer possibly lead to the condensation of water molecules. The carbonation reaction then accelerates as mediated by the as-produced liquid phase at the reaction interface, LHMH–LH(aq)–Li₂CO₃. Evaporation rate of the liquid phase depends on heating conditions. The evaporation rate also influences the counter diffusion rate of CO₂ into the surface product layer. Under these conditions, the overall reaction rate is controlled by the interrelationship between H₂O evolution and CO₂ intake. At the boiling point of the liquid phase, all the water molecules inside the reacting particle evaporate, and the thermal dehydration of LHMH is complete. The amount of residual LH in the reacting particle thus varies depending on CO₂ concentration and heating conditions for the temperatures below the boiling point. The residual LH reacts with CO₂ without a mediating liquid phase for higher temperatures consistent with carbonation of LH. Based on the phenomenological reaction model, the variation of overall behavior of the carbonation reaction of LHMH under linearly increasing temperature with changes in heating rate and CO₂ concentration can be interpreted as a physico-geometrical behavior regulated by the self-generated reaction conditions in the reacting particles.

■ ASSOCIATED CONTENT

■ Supporting Information

Figures S1–S13 and Tables S1–S4. This material is available free of charge via the Internet at <http://pubs.acs.org>.

■ AUTHOR INFORMATION

Corresponding Author

* Tel/Fax: +81-82-424-7092. E-mail: nkoga@hiroshima-u.ac.jp

Notes

The authors declare no competing financial interest.

■ ACKNOWLEDGMENTS

The present work was partially supported by a grant-in-aid for scientific research (A) (25242015), (B) (22300272), and (C) (25350202, 25350203) from the Japan Society for the Promotion of Science.

■ REFERENCES

- (1) Stanmore, B. R.; Gilot, P. Review—Calcination and Carbonation of Limestone during Thermal Cycling for CO₂ Sequestration. *Fuel Process. Technol.* **2005**, *86*, 1707–1743.
- (2) Essaki, K.; Kato, M.; Uemoto, H. Influence of Temperature and CO₂ Concentration on the CO₂ Absorption Properties of Lithium Silicate Pellets. *J. Mater. Sci.* **2005**, *40*, 5017–5019.
- (3) Zeman, F. Effect of Steam Hydration on Performance of Lime Sorbent for CO₂ Capture. *Int. J. Greenhouse Gas Control* **2008**, *2*, 203–209.
- (4) Materic, V.; Smedley, S. I. High Temperature Carbonation of Ca(OH)₂. *Ind. Eng. Chem. Res.* **2011**, *50*, 5927–5932.
- (5) Valverde, J. M.; Sanchez-Jimenez, P. E.; Perejon, A.; Perez-Maqueda, L. A. CO₂ Multicyclic Capture of Pretreated/Doped CaO in the Ca-Looping Process. Theory and Experiments. *Phys. Chem. Chem. Phys.* **2013**, *15*, 11775–11793.
- (6) Valverde, J. M.; Sanchez-Jimenez, P. E.; Perejon, A.; Perez-Maqueda, L. A. Role of Looping-Calcination Conditions on Self-Reactivation of Thermally Pretreated CO₂ Sorbents Based on CaO. *Energy Fuels* **2013**, *27*, 3373–3384.
- (7) Valverde, J. M.; Sanchez-Jimenez, P. E.; Perejon, A.; Perez-Maqueda, L. A. Constant Rate Thermal Analysis for Enhancing the Long-Term CO₂ Capture of CaO at Ca-Looping Conditions. *Appl. Energy* **2013**, *108*, 108–120.
- (8) Sanchez-Jimenez, P. E.; Valverde, J. M.; Perez-Maqueda, L. A. Multicyclic Conversion of Limestone at Ca-Looping Conditions: The Role of Solid-State Diffusion Controlled Carbonation. *Fuel* **2013**, <http://dx.doi.org/10.1016/j.fuel.2013.09.064>.
- (9) Kato, M.; Yoshikawa, S.; Nakagawa, K. Carbon Dioxide Absorption by Lithium Orthosilicate in a Wide Range of Temperature and Carbon Dioxide Concentrations. *J. Mater. Sci. Lett.* **2002**, *21*, 485–487.
- (10) Rodriguez-Mosqueda, R.; Pfeiffer, H. Thermokinetic Analysis of the CO₂ Chemisorption on Li₄SiO₄ by Using Different Gas Flow Rates and Particle Sizes. *J. Phys. Chem. A* **2010**, *114*, 4535–4541.
- (11) Avalos-Rendon, T.; Casa-Madrid, J.; Pfeiffer, H. Thermochemical Capture of Carbon Dioxide on Lithium Aluminates (LiAlO₂ and Li₅AlO₄): A New Option for the CO₂ Absorption. *J. Phys. Chem. A* **2009**, *113*, 6919–6923.
- (12) Ávalos-Rendón, T.; Lara, V. H.; Pfeiffer, H. CO₂ Chemisorption and Cyclability Analyses of Lithium Aluminate Polymorphs (α - and β -Li₅AlO₄). *Ind. Eng. Chem. Res.* **2012**, *51*, 2622–2630.
- (13) Nakagawa, K.; Ohashi, T. A Novel Method of CO₂ Capture from High Temperature Gases. *J. Electrochem. Soc.* **1998**, *145*, 1344–1346.
- (14) Alcérrec-Corte, I.; Fregoso-Israel, E.; Pfeiffer, H. CO₂ Absorption on Na₂ZrO₃: A Kinetic Analysis of the Chemisorption and Diffusion Processes. *J. Phys. Chem. C* **2008**, *112*, 6520–6525.
- (15) Martínez-dlCruz, L.; Pfeiffer, H. Microstructural Thermal Evolution of the Na₂CO₃ Phase Produced during a Na₂ZrO₃–CO₂ Chemisorption Process. *J. Phys. Chem. C* **2012**, *116*, 9675–9680.
- (16) Nikulshina, V.; Gálvez, M. E.; Steinfeld, A. Kinetic Analysis of the Carbonation Reactions for the Capture of CO₂ from Air via the Ca(OH)₂–CaCO₃–CaO Solar Thermochemical Cycle. *Chem. Eng. J.* **2007**, *129*, 75–83.
- (17) Prigiobbe, V.; Poletti, A.; Baciocchi, R. Gas–Solid Carbonation Kinetics of Air Pollution Control Residues for CO₂ Storage. *Chem. Eng. J.* **2009**, *148*, 270–278.
- (18) Montes-Hernandez, G.; Pommerol, A.; Renard, F.; Beck, P.; Quirico, E.; Brissaud, O. In situ Kinetic Measurements of Gas–Solid Carbonation of Ca(OH)₂ by Using an Infrared Microscope Coupled to a Reaction Cell. *Chem. Eng. J.* **2010**, *161*, 250–256.

- (19) Montes-Hernandez, G.; Chiriac, R.; Toche, F.; Renard, F. Gas–Solid Carbonation of $\text{Ca}(\text{OH})_2$ and CaO Particles under Non-Isothermal and Isothermal Conditions by Using a Thermogravimetric Analyzer: Implications for CO_2 Capture. *Int. J. Greenhouse Gas Control* **2012**, *11*, 172–180.
- (20) Rouchon, L.; Favregeon, L.; Pijolat, M. Analysis of the Kinetic Slowing Down during Carbonation of CaO by CO_2 . *J. Therm. Anal. Calorim.* **2013**, *113*, 1145–1155.
- (21) Beruto, D. T.; Botter, R. Liquid-Like H_2O Adsorption Layers to Catalyze the $\text{Ca}(\text{OH})_2/\text{CO}_2$ Solid–Gas Reaction and to Form a Non-Protective Solid Product Layer at 20°C . *J. Eur. Ceram. Soc.* **2000**, *20*, 497–503.
- (22) Dheilly, R. M.; Tudo, J.; Sebaïbi, Y.; Quéneudec, M. Influence of Storage Conditions on the Carbonation of Powdered $\text{Ca}(\text{OH})_2$. *Construct. Build. Mater.* **2002**, *16*, 155–161.
- (23) Seo, Y.; Jo, S. H.; Ryu, C. K.; Yi, C. K. Effects of Water Vapor Pretreatment Time and Reaction Temperature on CO_2 Capture Characteristics of a Sodium-Based Solid Sorbent in a Bubbling Fluidized-Bed Reactor. *Chemosphere* **2007**, *69*, 712–718.
- (24) Chen, M.; Wang, N.; Yu, J.; Yamaguchi, A. Effect of Porosity on Carbonation and Hydration Resistance of CaO Materials. *J. Eur. Ceram. Soc.* **2007**, *27*, 1953–1959.
- (25) Materić, V.; Edwards, S.; Smedley, S. I.; Holt, R. $\text{Ca}(\text{OH})_2$ Superheating as a Low-Attrition Steam Reactivation Method for CaO in Calcium Looping Applications. *Ind. Eng. Chem. Res.* **2010**, *49*, 12429–12434.
- (26) Blamey, J.; Lu, D. Y.; Fennell, P. S.; Anthony, E. J. Reactivation of CaO -Based Sorbents for CO_2 Capture: Mechanism for the Carbonation of $\text{Ca}(\text{OH})_2$. *Ind. Eng. Chem. Res.* **2011**, *50*, 10329–10334.
- (27) Montes-Hernandez, G.; Daval, D.; Chiriac, R.; Renard, F. Growth of Nanosized Calcite through Gas–Solid Carbonation of Nanosized Portlandite under Anisobaric Conditions. *Cryst. Growth Des.* **2010**, *10*, 4823–4830.
- (28) Besson, R.; Favregeon, L. Atomic-Scale Study of Calcite Nucleation in Calcium Oxide. *J. Phys. Chem. C* **2013**, *117*, 8813–8821.
- (29) Montes-Hernandez, G.; Daval, D.; Findling, N.; Chiriac, R.; Renard, F. Linear Growth Rate of Nanosized Calcite Synthesized via Gas–Solid Carbonation of $\text{Ca}(\text{OH})_2$ Particles in a Static Bed Reactor. *Chem. Eng. J.* **2012**, *180*, 237–244.
- (30) Ticich, T. M. Carbon Dioxide Absorbers: An Engaging Experiment for the General Chemistry Laboratory. *J. Chem. Educ.* **2011**, *88*, 189–191.
- (31) Williams, D. D.; Miller, R. R. Effect of Water Vapor on the $\text{LiOH}\text{--}\text{CO}_2$ Reaction. Dynamic Isothermal System. *Ind. Eng. Chem. Fundam.* **1970**, *9*, 454–457.
- (32) Boryta, D. A.; Maas, A. J. Factors Influencing Rate of Carbon Dioxide Reaction with Lithium Hydroxide. *Ind. Eng. Chem. Process Des. Dev.* **1971**, *10*, 489–494.
- (33) Wang, T. C.; Bricker, J. L. Combined Temperature and Water Vapor Effects on the Lithium Hydroxide–Carbon Dioxide Reaction in Underwater Life Support Systems. *Environ. Int.* **1979**, *2*, 425–430.
- (34) Zho, Z.; Chashchin, V. A.; Vishnyakov, A. V. Carbonization Kinetics of Lithium Hydroxide and Its Monohydrate. *Theor. Found. Chem. Eng.* **2007**, *41*, 577–584.
- (35) Tanaka, H.; Koga, N.; Galwey, A. K. Thermal Dehydration of Crystalline Hydrates: Microscopic Studies and Introductory Experiments to the Kinetics of Solid-State Reactions. *J. Chem. Educ.* **1995**, *72*, 251–256.
- (36) Alcock, N. Refinement of the Crystal Structure of Lithium Hydroxide Monohydrate. *Acta Crystallogr., Sect. B* **1971**, *27*, 1682–1683.
- (37) Kiat, J. M.; Boemare, G.; Rieu, B.; Aymes, D. Structural Evolution of LiOH : Evidence of a Solid–Solid Transformation toward Li_2O Close to the Melting Temperature. *Solid State Commun.* **1998**, *108*, 241–245.
- (38) Noda, S.; Nishioka, M.; Sadakata, M. Gas-Phase Hydroxyl Radical Emission in the Thermal Decomposition of Lithium Hydroxide. *J. Phys. Chem. B* **1999**, *103*, 1954–1959.
- (39) Mérawa, M.; Labeguerie, P.; Ugliengo, P.; Doll, K.; Dovesi, R. The Structural, Electronic and Vibrational Properties of LiOH and NaOH : An ab initio Study. *Chem. Phys. Lett.* **2004**, *387*, 453–459.
- (40) Koga, N.; Šesták, J.; Šimon, P. Some Fundamental and Historical Aspects of Phenomenological Kinetics in the Solid State Studied by Thermal Analysis. In *Thermal analysis of Micro, Nano- and Non-crystalline materials*; Šesták, J., Šimon, P., Eds.; Springer: Berlin, 2013; pp 1–28.
- (41) Koga, N. Ozawa's Kinetic Method for Analyzing Thermoanalytical Curves. *J. Therm. Anal. Calorim.* **2013**, *113*, 1527–1541.
- (42) Friedman, H. L. Kinetics of Thermal Degradation of Charring Plastics from Thermogravimetry, Application to a Phenolic Plastic. *J. Polym. Sci., Part C* **1964**, *6*, 183–195.
- (43) Ozawa, T. Non-Isothermal Kinetics and Generalized Time. *Thermochim. Acta* **1986**, *100*, 109–118.
- (44) Koga, N. Kinetic Analysis of Thermoanalytical Data by Extrapolating to Infinite Temperature. *Thermochim. Acta* **1995**, *258*, 145–159.
- (45) Gotor, F. J.; Criado, J. M.; Málek, J.; Koga, N. Kinetic Analysis of Solid-State Reactions: The Universality of Master Plots for Analyzing Isothermal and Nonisothermal Experiments. *J. Phys. Chem. A* **2000**, *104*, 10777–10782.
- (46) Koga, N.; Tanaka, H. Accommodation of the Actual Solid-State Process in the Kinetic Model Function. 1. Significance of the Nonintegral Kinetic Exponents. *J. Therm. Anal.* **1994**, *41*, 455–469.
- (47) Koga, N.; Maruta, S.; Kimura, T.; Yamada, S. Phenomenological Kinetics of the Thermal Decomposition of Sodium Hydrogencarbonate. *J. Phys. Chem. A* **2011**, *115*, 14417–14429.
- (48) Koga, N.; Tanaka, H. Effect of Sample Mass on the Kinetics of Thermal Decomposition of a Solid. Part 1. Isothermal Mass-Loss Process of Molten NH_4NO_3 . *Thermochim. Acta* **1992**, *209*, 127–134.
- (49) Koga, N.; Tanaka, H. Effect of Sample Mass on the Kinetics of Thermal Decomposition of a Solid. II. Isothermal Dehydration of $\text{Li}_2\text{SO}_4\text{--H}_2\text{O}$. *J. Therm. Anal.* **1993**, *40*, 1173–1179.
- (50) Koga, N.; Tanaka, H. Effect of Sample Mass on the Kinetics of Thermal Decomposition of a Solid. Part 3. Nonisothermal Mass-Loss Process of Molten NH_4NO_3 . *Thermochim. Acta* **1994**, *240*, 141–151.
- (51) Koga, N.; Criado, J. M. The Influence of Mass Transfer Phenomena on the Kinetic Analysis for the Thermal Decomposition of Calcium Carbonate by Constant Rate Thermal Analysis (CRTA) under Vacuum. *Int. J. Chem. Kinet.* **1998**, *30*, 737–744.
- (52) Koga, N.; Criado, J. M. Influence of the Particle Size Distribution on the CRTA Curves for the Solid-State Reactions of Interface Shrinkage. *J. Therm. Anal.* **1997**, *49*, 1477–1484.
- (53) Effenberger, H.; Zemann, J. Verfeinerung der Kristallstruktur des Lithiumcarbonates, Li_2CO_3 . *Z. Kristallogr.* **1979**, *150*, 133–138.
- (54) Tanaka, H.; Koga, N. Kinetics of the Thermal Dehydration of Potassium Copper(II) Chloride Dihydrate. *J. Phys. Chem.* **1988**, *92*, 7023–7029.
- (55) Koga, N.; Tanaka, H. Kinetic and Morphological Studies of the Thermal Dehydration of α -Nickel(II) Sulfate Hexahydrate. *J. Phys. Chem.* **1994**, *98*, 10521–10528.
- (56) Koga, N.; Tanaka, H. A Physico-Geometric Approach to the Kinetics of Solid-State Reactions as Exemplified by the Thermal Dehydration and Decomposition of Inorganic Solids. *Thermochim. Acta* **2002**, *388*, 41–61.
- (57) Sánchez-Jiménez, P. E.; Perejón, A.; Criado, J. M.; Diáñez, M. J.; Pérez-Maqueda, L. A. Kinetic Model for Thermal Dehydrochlorination of Poly(Vinyl Chloride). *Polymer* **2010**, *51*, 3998–4007.
- (58) Sánchez-Jiménez, P. E.; Pérez-Maqueda, L. A.; Perejón, A.; Criado, J. M. Nanoclay Nucleation Effect in the Thermal Stabilization of a Polymer Nanocomposite: A Kinetic Mechanism Change. *J. Phys. Chem. C* **2012**, *116*, 11797–11807.
- (59) Koga, N.; Suzuki, Y.; Tatsuoka, T. Thermal Dehydration of Magnesium Acetate Tetrahydrate: Formation and in situ Crystallization of Anhydrous Glass. *J. Phys. Chem. B* **2012**, *116*, 14477–14486.

- (60) Koga, N.; Yamada, S.; Kimura, T. Thermal Decomposition of Silver Carbonate: Phenomenology and Physicogeometrical Kinetics. *J. Phys. Chem. C* **2013**, *117*, 326–336.
- (61) Wada, T.; Koga, N. Kinetics and Mechanism of the Thermal Decomposition of Sodium Percarbonate: Role of the Surface Product Layer. *J. Phys. Chem. A* **2013**, *117*, 1880–1889.
- (62) Šesták, J.; Berggren, G. Study of the Kinetics of the Mechanism of Solid-State Reactions at Increasing Temperatures. *Thermochim. Acta* **1971**, *3*, 1–12.
- (63) Šesták, J. Diagnostic Limits of Phenomenological Kinetic Models Introducing the Accommodation Function. *J. Therm. Anal.* **1990**, *36*, 1997–2007.
- (64) Málek, J.; Criado, J. M. Empirical Kinetic Models in Thermal Analysis. *Thermochim. Acta* **1992**, *203*, 25–30.
- (65) Perez-Maqueda, L. A.; Criado, J. M.; Sanchez-Jimenez, P. E. Combined Kinetic Analysis of Solid-State Reactions: A Powerful Tool for the Simultaneous Determination of Kinetic Parameters and the Kinetic Model without Previous Assumptions on the Reaction Mechanism. *J. Phys. Chem. A* **2006**, *110*, 12456–12462.
- (66) Šesták, J. Rationale and Fallacy of Thermoanalytical Kinetic Patterns. *J. Therm. Anal. Calorim.* **2011**, *110*, 5–16.
- (67) Koga, N. A Review of the Mutual Dependence of Arrhenius Parameters Evaluated by the Thermoanalytical Study of Solid-State Reactions: The Kinetic Compensation Effect. *Thermochim. Acta* **1994**, *244*, 1–20.
- (68) Liu, L.; Guo, Q.-X. Isokinetic Relationship, Isoequilibrium Relationship, and Enthalpy–Entropy Compensation. *Chem. Rev.* **2001**, *101*, 673–696.
- (69) Galwey, A. K.; Mortimer, M. Compensation Effects and Compensation Defects in Kinetic and Mechanistic Interpretations of Heterogeneous Chemical Reactions. *Int. J. Chem. Kinet.* **2006**, *38*, 464–473.
- (70) L'vov, B. V.; Galwey, A. K. Interpretation of the Kinetic Compensation Effect in Heterogeneous Reactions: Thermochemical Approach. *Int. Rev. Phys. Chem.* **2013**, *32*, 515–557.